Grid Current Control for Active-Front-End Electric Propulsion Systems in AC Ship Microgrids

Diego Pérez-Estévez, *Member, IEEE*, Jesús Doval-Gandoy, *Member, IEEE* and Alberto Crego-Lourido

***Abstract*—This article proposes a finite control set (FCS) current controller for grid-tied converters, specifically tailored to meet the characteristics of AC ship microgrids in all-electric ships (AESs). Contrarily to a pulse width modulator (PWM)-based design, which often employs an LCL filter, the proposal is able to meet applicable harmonic regulations using an L filter with the same total inductance as the LCL filter and the same switching frequency required by PWM-based solutions. Moreover, the proposed design provides a low sensitivity in a wide frequency range from DC to the switching frequency of the power converter. This low sensitivity permits to quickly attenuate low-order disturbances and it is particularly convenient in marine applications with a weak grid, where the frequent connection and disconnection of high power nonlinear loads can significantly affect the voltage waveform quality.**

***Index Terms*—Current controller, L, LCL, PWM, FCS, inverter, weak grid, harmonics, state-space control.**

I. Introduction

Ship electrification is steadily gaining attention thanks to environmental and economical reasons as well as recent technology improvements in electric power conversion that originate from an intensive research effort throughout the last century [1]–[5]. In this process, the concept of all-electric ship (AES) arises as a solution in which ship loads are powered from the same electrical source as the propulsion system. AESs do not require a separate generation system for the ship loads and the electric propulsion. Such configuration results in an electrical plant that behaves as a single complex microgrid where electric demand can experience large variations compared to the total available power. Sometimes, an energy storage system is incorporated in order to stabilize the microgid and further optimize operative costs [6]. An energy storage system can improve the fuel economy of diesel generators by regulating their load demand [7] and provide emergency power promptly whenever necessary [8]. However, this type of marine grid presents specific characteristics that challenge the integration of modern power converters [3], [9], [10], specially when the support of an energy storage system (ESS) to stabilize and strengthen the grid is not available.

In a typical all-electric ship, the electrical plant is composed of several generators connected in parallel to form a microgrid. Power is delivered to the loads and the electric propulsion system (EPS) using a radial electric distribution network that often incorporates transformers in order to generate different voltage levels required by the loads. The propulsion system is often the most critical load in terms of grid current distortion and its impact in the grid voltage quality. For low voltage applications and rated power below $10\ \mathrm{MW}$, the EPS is usually composed of a back-to-back power converter that interfaces the electric propulsion motors with the grid, due to its high power demand compared to the generators rating and the rest of the ship loads. In such power range, the grid-side of the back-to-back converter frequently employs an active front end (AFE) with an LCL coupling filter working as a rectifier.

The amplitude of the current harmonics allowed in a grid connection typically depends on the grid short circuit ratio (SCR) because the degradation of the grid voltage when distorted or nonlinear loads are connected increases when the value of the grid SCR decreases. For this reason, the standard [11] recommends to apply more stringent harmonic limits to weak grids. An example of a weak grid with a high penetration of nonlinear loads and power converters is found in AES. This type of grid has a small size compared to the number of loads, and some of the loads, such as the EPS, can have a power demand comparable to the total generation power available, which results in a very low grid short circuit ratio. Such weak grid impedance combined with a high penetration of switching loads can lead to the appearance of electrical resonances and waveform quality problems. Electrical resonances can be excited by any switching event in the plant or a switching power converter.

Marine power conversion equipment often has to meet specific grid voltage and current quality requirements, which can be further classified in civil [11]–[14] and military standards [15]–[18]. Compared to the harmonic limits recommended for civil applications, the standards [15] and [16] define more stringent limits for low order harmonics, below one kilohertz, and extend the coverage to higher frequencies up to ten kilohertzs. These limits favor the use of fully controlled power converters to interface with the grid, in place of more traditional uncontrolled or semi-controlled structures using diodes or thyristors. Moreover, these standards [12], [13], [15]–[17] apply the same limits to even and odd harmonics, which simplifies compliance of power converters with direct controllers that do not use pulse width modulator (PWM) but

Manuscript received xxxxx; revised xxxxx; accepted xxxxx. Date of current version xxxxx. This work was supported in part by the Spanish State Research Agency (AEI) under project PID2019-105612RB-I00/AEI/10.13039/501100011033 and in part by the Government of Galicia under the project GPC-ED431B 2020/03.

D. Pérez-Estévez and J. Doval-Gandoy are with CINTECX, Universidade de Vigo, Applied Power Electronics Technology research group (APET), 36310 Vigo, Spain (e-mail: dieperez@uvigo.es; jdoval@uvigo.es).

A. Crego-Lourido is with Navantia, Ferrol, Spain (e-mail: acrego@navantia.es).

Color versions of one or more of the figures in this paper are available online at http://ieeexplore.ieee.org.

Digital Object Identifier xxxxx

use finite control set (FCS) operation [19]–[23].

On the one hand, PWM-based power converters typically generate low-order harmonics and high frequency or switching harmonics. The main low-order harmonics are typically located at odd harmonic frequencies. The switching operation of the converter can generate significantly large current harmonics at high frequencies and the instalation of an LCL filter can facilitate the circulation of other loads current harmonics [24]. The amplitude of these switching harmonics greatly depends on the grid impedance. The location of the switching harmonics depends on the switching frequency selected for the PWM. By selecting a switching frequency that is a triple odd multiple of the fundamental grid frequency, the switching harmonics of a PWM-based converter are also placed at odd harmonic frequencies. On the other hand, power converters with direct controllers and a FCS operation do not contain harmonics in the strict sense, because they do not generate a periodic waveform. Converters with a direct controller, such as direct torque control (DTC) [25], direct power control (DPC) [26], direct model predictive controller (MPC) [27], or noise shaping [23], generate switching noise that is spread throughout a wide and continuous frequency range instead of it being concentrated at a set of frequencies. Therefore a direct application of the harmonic limits defined in [11] and [14] can be difficult. This problem has been recognized in [21] and [23], where the use of a FCS operation is not recommended for terrestrial grid-tied inverters due to the difficulty of meeting the harmonic limits established in terrestrial grid codes, which define much more stringent limits for even harmonics than for odd harmonics.

Another important advantage of a FCS operation compared to a PWM-based design arises when multiple converters operate in parallel. In order to achieve compliance with marine grid standards, the grid voltage has also to meet harmonic limits. When several power converters operate in parallel, it is possible to surpass the grid voltage distortion limits even if the individual converters meet their individual current harmonic limits. When a specific harmonic number is generated by several PWM-based converters, the amplitude of the resultant harmonic is calculated by adding the harmonic amplitude of each individual converter in phase, in order to assume a worst case scenario. Contrarily, the total distortion generated by converters with a FCS operation is calculated by adding in quadrature the distortion of each individual converter, which reduces by a factor of $\sqrt{2}$ the distortion generated compared to a PWM-based design. Additionally, since distortion of a converter with a FCS operation is not concentrated at specific harmonic numbers, compliance with individual harmonic limits can be more easily achieved and the risk of exciting unmodeled resonance in the electrical plant is minimized.

This article proposes a FCS current controller for grid-tied converters, specifically tailored to meet the characteristics of AC ship microgrids in AES. Contrarily to a PWM-based design which often employs an LCL filter, the proposal is able to meet applicable harmonic regulation using an L filter with the same total inductance as the LCL filter required by PWM-based solutions and the same average switching frequency. The proposal requires a more complex design process and a slightly higher computational load, compared to a conventional PWM-based power converter with a proportional-integral (PI) or proportional-resonant (PR) controller. However, with the advent of micro-controller technology, modern embedded controllers significantly exceed the capabilities required by the additional computational burden. The rest of this paper is organized in the following manner. Section II derives a plant and a disturbance model used to mathematically describe a marine grid in an AES. Such model is used next to design the proposed controller. Section III introduces the controller architecture and design process. Section IV explains the theory of operation of the controller and presents a theoretical analysis that compares the performance of the proposal to a PWM-based design. In Section V, simulation and experimental results that validate the theory are presented. Finally, Section VI concludes this work.

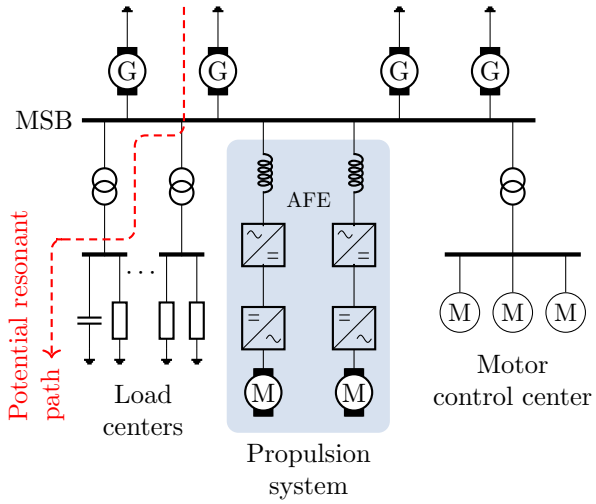

Fig. 1. Simplified single-line diagram with a potential parallel resonant situation in an electrical power plant of an all-electric ship (AES) ship with an electric propulsion system (EPS) that includes an active front end (AFE).

II. Electric Plant Model and Disturbance Model

In order to design a current controller for an AFE that is part of an EPS in an AES, a model of an electrical plant is first defined. An electrical plant in an AES is typically composed of several generators operating in parallel and connected to one or several main switching boards (MSBs). The MSBs feed a microgrid using a radial electric distribution network that delivers power to load centers and motor control centers. Fig. 1 shows a single-line diagram of a typical electric plant in an AES. The plant seen by the current controller in an AFE is determined by the impedance of the coupling filter (L or LCL filter) and the grid impedance at the point of common coupling (PCC) Z_{g}, as illustrated in Fig. 2. In marine applications, the grid impedance can change significantly depending on the electric plant configuration. The plant configuration is defined by the number of generators and loads in operation.

Since the grid impedance can experience large variations, the controller should not rely on an accurate plant model to operate. The plant model used by the proposal is a second-order discrete-time model. Such low-order model describes

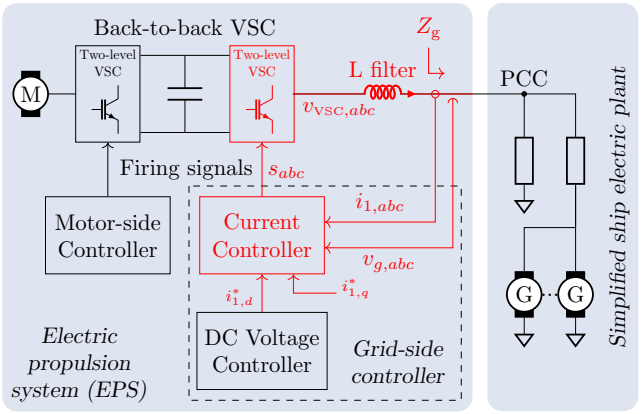

Fig. 2. Detailed structure of an electric propulsion system (EPS) that contains an active front end (AFE) connected to the ship grid. Grid-side current regulated by a current controller with a finite control set (FCS) operation, i.e., the current controller directly generates the firing signals that control the VSC.

the response of an L filter and the phase lag introduced by the computational and modulation delays. This model does not describe the effect of resonances that may appear in the grid impedance due to the interaction between capacitive loads and inductive elements such as transformers and cables, as illustrated in Fig. 1. These phenomena depend on the particular loading conditions of the electrical plant and should not be included in the time-invariant model used by the controller due to its unpredictability. Despite them not being included in the model, the robustness of the controller to such model changes is also studied.

In the following, the mathematical derivation of the plant model used by the controller is presented. A state-space representation is selected for the plant model because it facilitates the design of the controller, which uses a state feedback structure. The modeling process is carried out in the $\alpha\beta$ frame and consists of three steps. For simplicity, if no reference frame is explicitly indicated in the name of a variable, the $\alpha\beta$ frame is assumed by default. First, a continuous-time model that relates the grid current $i_1(t)$ to the VSC output voltage $v_{\text{VSC}}(t)$ is defined. Next, such model is discretized using a zero-order-hold (ZOH). Such discretization method accurately describes the FCS operation of the VSC and the sampling process carried out by the digital controller. Finally, a one-sample input delay is added to the model so as to account for the lag caused by the computational delay.

The continuous-time plant model is

$$\frac{\mathrm{d}\, i_1(t)}{\mathrm{d}t} = \frac{-R_\mathrm{f}}{L_\mathrm{f}} i_1(t) + \frac{1}{L_\mathrm{f}} v_{\text{VSC}}(t). \tag{1}$$

Hence, in state-space notation, the system state matrix $\mathbf{A}^{\text{L}}_{\text{cont}}$ is $-R_\mathrm{f}/L_\mathrm{f}$; the input matrix $\mathbf{B}^{\text{L}}_{\text{cont}}$ is $1/L_\mathrm{f}$; the output matrix $\mathbf{C}^{\text{L}}_{\text{cont}}$ is equal to one; and the state vector $\mathbf{x}^{\text{L}}_{\text{cont}}$ only contains one state variable, the grid current $i_1(t)$. This equation does not include the grid voltage v_g as an input to the model because the proposed controller assumes the grid voltage is an unknown disturbance.

Next, the continuous-time model (1) is discretized using a ZOH equivalent [28]. The resultant matrices of the discrete-time state-space model for the L filter are

$$\begin{aligned}
\mathbf{A}^{\text{L}}_{\text{disc}} &= \exp\left\{\mathbf{A}^{\text{L}}_{\text{cont}}\, T_s\right\},\\
\mathbf{B}^{\text{L}}_{\text{disc}} &= {\mathbf{A}^{\text{L}}_{\text{cont}}}^{-1}(\exp\{\mathbf{A}^{\text{L}}_{\text{cont}} T_s\} - 1)\mathbf{B}^{\text{L}}_{\text{cont}},\\
\mathbf{C}^{\text{L}}_{\text{disc}} &= \mathbf{C}^{\text{L}}_{\text{cont}}.
\end{aligned} \tag{2}$$

Finally, a one-sample input (computational) delay is added to the discrete-time model. The augmented system model is

$$\underbrace{\begin{bmatrix}\mathbf{x}^{\text{L}}_{\text{disc}}(k+1)\\ v_d(k+1)\end{bmatrix}}_{\mathbf{x}_{\text{plant}}(k+1)} = \underbrace{\begin{bmatrix}\mathbf{A}^{\text{L}}_{\text{disc}} & \mathbf{B}^{\text{L}}_{\text{disc}}\\ \mathbf{0} & 0\end{bmatrix}}_{\mathbf{A}_{\text{plant}}} \underbrace{\begin{bmatrix}\mathbf{x}^{\text{L}}_{\text{disc}}(k)\\ v_d(k)\end{bmatrix}}_{\mathbf{x}_{\text{plant}}(k)} + \underbrace{\begin{bmatrix}\mathbf{0}\\ 1\end{bmatrix}}_{\mathbf{B}_{\text{plant}}} v(k)$$

$$i_1(k) = \underbrace{\begin{bmatrix}\mathbf{C}^{\text{L}}_{\text{disc}} & 0\end{bmatrix}}_{\mathbf{C}_{\text{plant}}} \underbrace{\begin{bmatrix}\mathbf{x}^{\text{L}}_{\text{disc}}(k)\\ u_d(k)\end{bmatrix}}_{\mathbf{x}_{\text{plant}}(k)}. \tag{3}$$

In addition to the plant model, the controller also uses a disturbance model. The disturbance model adds degrees of freedom to the system and it permits to adjust more precisely the disturbance rejection capability of the controller. In particular, the proposal uses a fourth-order disturbance model that is composed of two resonant controllers (RCs). This choice permits to independently adjust the attenuation of disturbances at two frequencies. An RC tuned at the fundamental grid frequency C_{low}:

$$C_{\text{low}}(s) = \frac{K_{\text{low}}}{s^2 - \omega^2_{\text{low}}}, \tag{4}$$

and a detuned RC placed at a high frequency C_{high}:

$$C_{\text{high}}(s) = \frac{K_{\text{high}}}{s^2 + 2\zeta\omega_{\text{high}} s + \omega_{\text{high}}}. \tag{5}$$

Such disturbance model filters the grid current error $e = i_1^* - i_1$ and selectively amplifies some frequencies. The output of the disturbance model is the weighted grid-current error w. The disturbance model transfer function is obtained by adding the two RC:

$$C_{\text{dist}}(s) = \frac{w(t)}{e(t)} = C_{\text{low}}(s) + C_{\text{high}}(s) = \tag{6}$$

$$= \frac{n_1 s^3 + n_2 s^2 + n_3 s + n_4}{s^4 + d_1 s^3 + d_2 s^2 + d_3 s + d_4}. \tag{7}$$

Fig. 3(a) shows a block diagram representation of (6).

In order to use the previous disturbance model in the

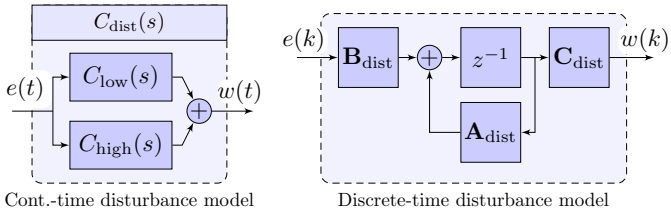

Fig. 3. Disturbance models. (a) Continuous-time transfer-function model. (b) Discrete-time state-space model.

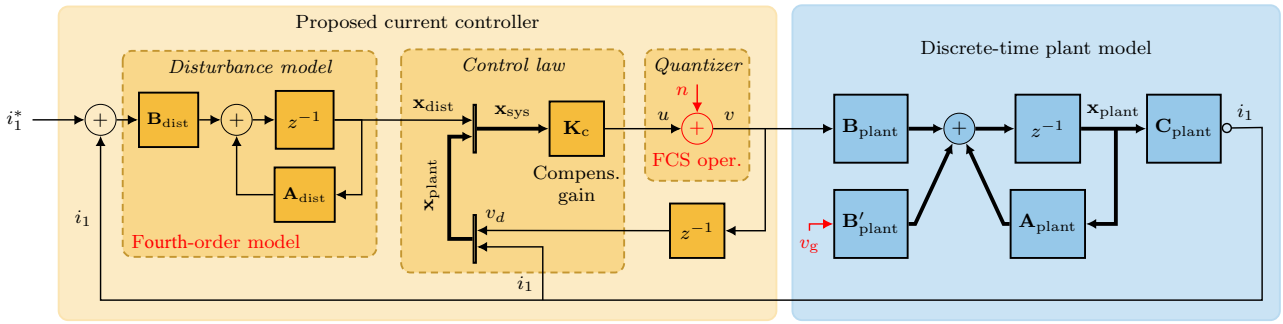

Fig. 4. Detailed structure of the proposed current controller and the discrete-time plant model in the $\alpha\beta$ frame. Thin lines denote complex-valued scalar variables and thick lines denote complex valued vector variables.

proposed controller, the transfer function representation (6) is expressed as a direct canonical realization in state-space notation. Such realization choice ensures that the first state variable in the disturbance model is equal to the output of the model w.

The state-space model matrices $\mathbf{A}_{\text{c,dist}}$, $\mathbf{B}_{\text{c,dist}}$, and $\mathbf{C}_{\text{c,dist}}$ that model (6) in a direct canonical realization are

$$\mathbf{A}_{\text{c,dist}} = \begin{bmatrix} -d_1 & 1 & 0 & 0 \\ -d_2 & 0 & 1 & 0 \\ -d_3 & 0 & 0 & 1 \\ -d_4 & 0 & 0 & 0 \end{bmatrix}$$

$$\mathbf{B}_{\text{c,dist}} = \begin{bmatrix} n_1 \\ n_2 \\ n_3 \\ n_4 \end{bmatrix}$$

$$\mathbf{C}_{\text{c,dist}} = \begin{bmatrix} 1 & 0 & 0 & 0 \end{bmatrix}. \tag{8}$$

Next, similarly to the modeling process carried out to obtain the discrete-time plant model, the disturbance model matrices $\mathbf{A}_{\text{c,dist}}$, $\mathbf{B}_{\text{c,dist}}$, and $\mathbf{C}_{\text{c,dist}}$ are discretized using a ZOH equivalent. The obtained discrete-time disturbance model matrices are

$$\begin{aligned} \mathbf{A}_{\text{dist}} &= \exp\left\{\mathbf{A}_{\text{c,dist}}\, T_s\right\} \\ \mathbf{B}_{\text{dist}} &= {\mathbf{A}_{\text{c,dist}}}^{-1}(\exp\{\mathbf{A}_{\text{c,dist}} T_s\} - \mathbf{I_4})\mathbf{B}_{\text{c,dist}} \\ \mathbf{C}_{\text{dist}} &= \mathbf{C}_{\text{c,dist}}, \end{aligned} \tag{9}$$

where $\mathbf{I_4}$ is the 4×4 identity matrix.

The resultant discrete-time disturbance model is

$$\begin{aligned} \mathbf{x}_{\text{dist}}(k+1) &= \mathbf{A}_{\text{dist}}\, \mathbf{x}_{\text{dist}}(k) + \mathbf{B}_{\text{dist}}\, e(k) \\ w(k) &= \mathbf{C}_{\text{dist}}\, \mathbf{x}_{\text{dist}}(k) \\ \mathbf{x}_{\text{dist}} &= \begin{bmatrix} w & w_a & w_b & w_c \end{bmatrix}^{\text{T}}, \end{aligned} \tag{10}$$

where w, w_a, w_b, and w_c are the state variables. It should be noted that the first state variable w is equal to the output of the disturbance model, cf. (6). Fig. 3(b) shows a graphical representation of the disturbance model as included in the proposed controller.

III. Controller Structure

The proposed controller uses a state-space structure. There are three main components in this controller structure. These three components are the control law, the disturbance model, and the quantizer. Contrarily to a traditional design, the proposal replaces the PWM with a quantizer, as shown in Fig. 4.

The control law changes the open-loop dynamics of the plant and the disturbance model to the desired closed-loop dynamics. The control law calculates the controller output voltage u by multiplying the system state vector by the compensator gain $\mathbf{K}_{\text{c}}$:

$$u = \mathbf{K}_{\text{c}}\, \mathbf{x}_{\text{sys}} = \mathbf{K}_{\text{c}} \begin{bmatrix} \mathbf{x}_{\text{dist}} \\ \mathbf{x}_{\text{plant}} \end{bmatrix} = \mathbf{K}_{\text{c}} \begin{bmatrix} \mathbf{x}_{\text{dist}} \\ i_1 \\ v_d \end{bmatrix}, \tag{11}$$

where the system vector $\mathbf{x}_{\text{sys}}$ is constructed by joining the disturbance state vector $\mathbf{x}_{\text{dist}}$ and the plant state vector $\mathbf{x}_{\text{plant}}$. The plant state vector is composed of two variables, namely, the previous controller output voltage v_d and the measured grid current i_1.

The disturbance model (10) contains four resonant poles that accumulates the current error $i_1 - i_1^*$ in the disturbance state vector $\mathbf{x}_{\text{dist}}$. A current error appears due to disturbances, such as the grid voltage v_g, and the the VSC switching noise n. It should be noticed that the proposed controller does not include a feedforward of the grid voltage. The grid voltage is an unmodeled disturbance from the point of view of the controller. The estimated disturbance state vector is passed down to the control law in order to be compensated or attenuated.

The last element, the quantizer, simply converts the controller reference voltage u to a suitable voltage reference v that can be generated by the VSC and applied at the plant input. Such conversion is equivalent to the addition of a known noise disturbance n to u:

$$v = u + n. \tag{12}$$

The noise disturbance n corresponds to the VSC switching noise. For example, in a two-level VSC, the VSC can only generate, between commutations, one of the seven voltages that are denoted as v_i with $i = 1, 2, \cdots, 7$, in Fig. 5.

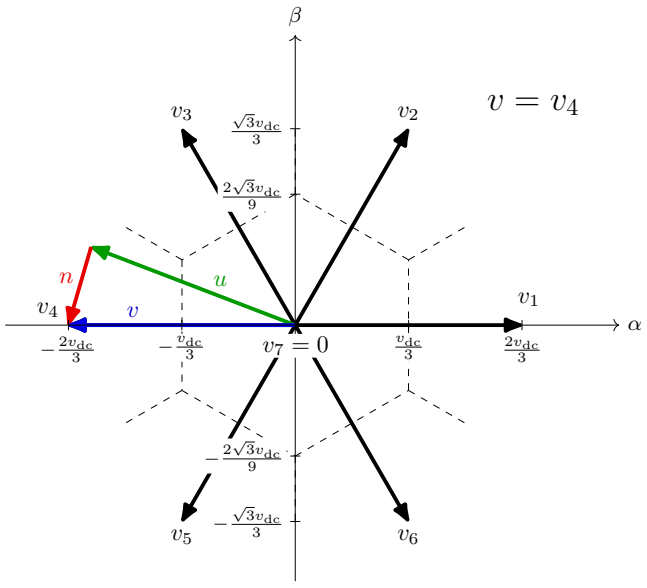

Fig. 5. Graphical representation in the $\alpha\beta$ frame of the Voronoi regions associated to each of the switching states v_i with $i = 1, 2, \cdots, 8$ of a two-level VSC and example of the complex-valued signals involved in the quantization process, namely, the linear controller output voltage u, the VSC output voltage v, and the switching (or quantization) noise n.

Therefore, if the control law commands a voltage vector u different from the previous seven voltage vectors, the VSC output voltage necessarily must contain an undesired switching noise n. The quantizer chooses the switching state that results in the least magnitude for n at every sampling period. The following section explains how the control law of the state space controller is designed so as to minimize the effect of unmeasured disturbances such as the grid voltage v_g and known disturbances like the VSC switching noise n.

IV. NTF Design by Optimal Pole Placement

The noise transfer function (NTF) defines the spectral shape of the switching noise generated by the VSC and also indicates the response of the controller to other disturbances, such as harmonics in the grid voltage or a grid voltage sag. Specifically, the noise transfer function (NTF) defines the amplitude of the plant input voltage as a function of the input disturbance n:

$$\text{NTF}(f) = v(f)/n(f). \tag{13}$$

The name for the NTF has been borrowed from the microelectronics field, where it is used as part of the optimization of delta-sigma data converters [29].

Within certain fundamental constraints, the designer can adjust the shape of the NTF in order to achieve the best performance. Ideally, the NTF magnitude should be as low as possible in order to eliminate the effect of disturbances such as n. This section describes the design criterion followed by the proposal and explains an unavoidable fundamental constraint that any NTF should meet.

During steady-state operation, an important figure of merit in a current controller is the amount of current distortion. The current distortion appears due to numerous reasons and can be classified into two main types, namely, low-order harmonics and high-frequency switching ripple.

On the one hand, low-order current harmonics can be caused by a distorted grid voltage, the dead-time introduced in the turn on of the VSC switching devices, and other non-linearities in the VSC or the filter elements, such as saturation of magnetic components. Typically, this distortion is eliminated by placing an integral or resonant action in the current controller at a set of harmonic frequencies, such as the fifth and seventh harmonics, which results in a zero sensitivity to disturbances at such frequencies. Contrarily to such traditional design, the proposed design provides a low sensitivity in a wide frequency range from DC to the switching frequency of the power converter. This permits to quickly attenuate low-order disturbances and is particularly convenient in marine applications with a weak grid, where the frequent connection and disconnection of high power nonlinear loads can significantly affect the voltage waveforms quality.

On the other hand, high frequency disturbances, such as the VSC switching ripple, are typically attenuated by the coupling filter because they are located outside the bandwidth of the discrete-time controller. There are two types of filters frequently used to couple a VSC to the grid, namely, an L filter and an LCL filter. The L filter steadily increases its impedance from DC up to its series resonance frequency, which for iron core inductors is often located around 100 kHz. Contrarily to a conventional design, the proposed controller has a bandwidth larger than the switching frequency and is able to attenuate the VSC switching noise.

Ideally, the controller should attenuate disturbances at all frequencies as much as possible, in order to meet applicable voltage and current harmonic limits, cf. Fig. 6(a). This harmonic limits extend up to the 100th harmonic, so as to include the high frequency switching harmonics that PWM-based power converters introduce. However, the disturbance rejection capability of any linear controller must meet Bode's integral theorem [30]. Such theorem states that, in a linear controller, there is an unavoidable tradeoff between disturbance rejection and disturbance amplification. In order to attenuate disturbances at a certain frequency range, the controller must necessarily amplify disturbances at other frequencies.

Applicable current harmonic limits in marine applications define a constant amplitude threshold for current distortion at frequencies below 1.92 kHz, as illustrated in Fig. 6. In an L filter, the filter impedance increases linearly with frequency in such frequency range; therefore, the shape of an ideal NTF should match the slope of the filter impedance in such frequency range, as illustrated in Fig. 7(a), in order to achieve a current distortion with a flat frequency response that matches the constant amplitude limits:

$$i_1(f) = \left.\frac{v(f)}{Z_{\text{L}}(f)}\right|_{v_g=0} = \frac{\text{NTF}(f)\cdot n(f)}{Z_{\text{L}}(f)}. \tag{14}$$

Above 1.92 kHz, the applicable current harmonic limits decrease with frequency; therefore, the response of an ideal NTF should level off at such frequency. In this manner, the increase in impedance of the L filter combined with constant amplitude

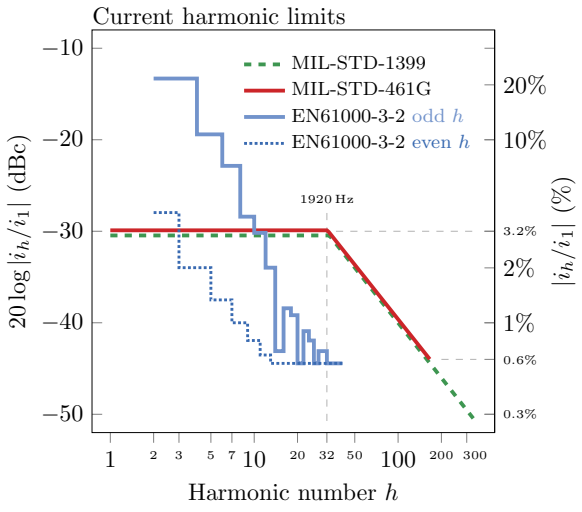

(a)

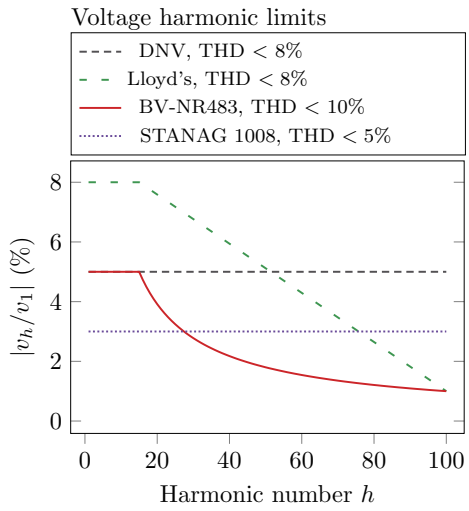

(b)

Fig. 6. Harmonic limits commonly adopted in electrical grids in AES ships. (a) Current harmonics of individual equipment (P >1 kVA and $i_1 > 1$ A). (b) Voltage harmonics.

voltage disturbances results in a current distortion decreasing with frequency. Fig. 7(a) shows an example of an ideal NTF that matches the design criteria explained before.

The proposed controller is linear, cf. Fig. 4. Applying linear theory operations to Fig. 4, an expression for the NTF is obtained. Such mathematical expression is a quotient of two polynomials where the roots of the denominator polynomial (NTF poles) are the system closed-loop poles and the roots of the numerator polynomial (NTF zeros) are the plant and disturbance model poles. By defining the position of the NTF roots the designer can control the shape of the NTF.

On the one hand, the designer has some control over some of the NTF disturbance zeros. Some zeros are located in the positions assigned to the disturbance model poles. The remaining NTF zeros cannot be positioned by the designer and they are determined by the setup parameters. These plant-dependent NTF zeros appear in the same location as the open-loop plant poles. In order to achieve the previously described design requirements, this proposal uses a disturbance model that consists of two resonant controllers (RCs), namely, an RC tuned at the fundamental grid frequency C_{low} and a detuned RC placed at high frequencies C_{high}. C_{low} introduces a pair of zeros at the fundamental grid frequency and C_{high} flattens the magnitude of the NTF at high frequencies, as shown in Fig. 7(b). By detuning the high-frequency resonant controller, i.e., by adding a small damping to the resonant poles of the controller, the controller action is spread over a wider frequency range arround f_{high} instead of targeting a narrow frequency range, cf. Fig. 7(b). This design choice helps to achieve compliance with harmonic distortion limits at high frequencies. Table I summarizes the location of the NTF zeros.

TABLE I
NOISE TRANSFER FUNCTION (NTF) ZEROS

	Position in the z-plane
Plant model	Open-loop plant poles become NTF zeros.
	$z_1^{\text{NTF}} = p_1^{ol} = \exp\left[2\pi\, T_s\, R_f/Lf\right]$
	$z_2^{\text{NTF}} = p_2^{ol} = 0$
Disturb. model	Open-loop disturbance poles becomes NTF zeros.
	$z_{3,4}^{\text{NTF}} = p_{3,4}^{ol} = \exp[\pm j\, 2\pi f_{\text{low}}\, T_s]$
	$z_{5,6}^{\text{NTF}} = p_{5,6}^{ol} = e^{-(\zeta 2\pi f_{\text{high}} \pm j 2\pi f_{\text{high}}\sqrt{1-\zeta^2})T_s}$

On the other hand, the designer has full control over the location of the NTF poles. The designer can place the NTF poles, which are also the system poles, at any location in the z plane by choosing a suitable compensator gain $\mathbf{K_c}$ (see control law in Fig. 4). The NTF has six poles as a result of using a forth-order disturbance model and a second-order plant model. A manual or direct placement of the six NTF poles is a challenging task. It is not simple to know beforehand which set of closed-loop pole locations yield a good performance in terms of disturbance rejection capability.

In a previous application of this novel type of linear FCS controller [23], a direct pole-placement technique was used to calculate the compensator gain $\mathbf{K_c}$, because in such application a simple first-order disturbance model was implemented. In this proposal, the compensator gain is calculated using a linear-quadratic regulator (LQR) technique. This simplifies the design process because it permits to automatically establish the closed-loop pole locations by simply specifying two weighting factors.

A. Compensator Design Using LQR Theory

LQR theory calculates a compensator gain that is optimal according to the following cost function:

$$J = \sum_{n=1}^{\infty} \left[\mathbf{x}_{\text{sys}}^{\mathbf{T}}(n)\, \mathbf{Q}\, \mathbf{x}_{\text{sys}}(n) + u^2(n)\, \mathbf{R}\right], \qquad (15)$$

where $\mathbf{Q}$ and $\mathbf{R}$ are state and control weighting matrices, respectively. This cost function measures the error in the system state variables and the controller effort. If the value of the elements of $\mathbf{Q}$ are increased, then the controller achieves

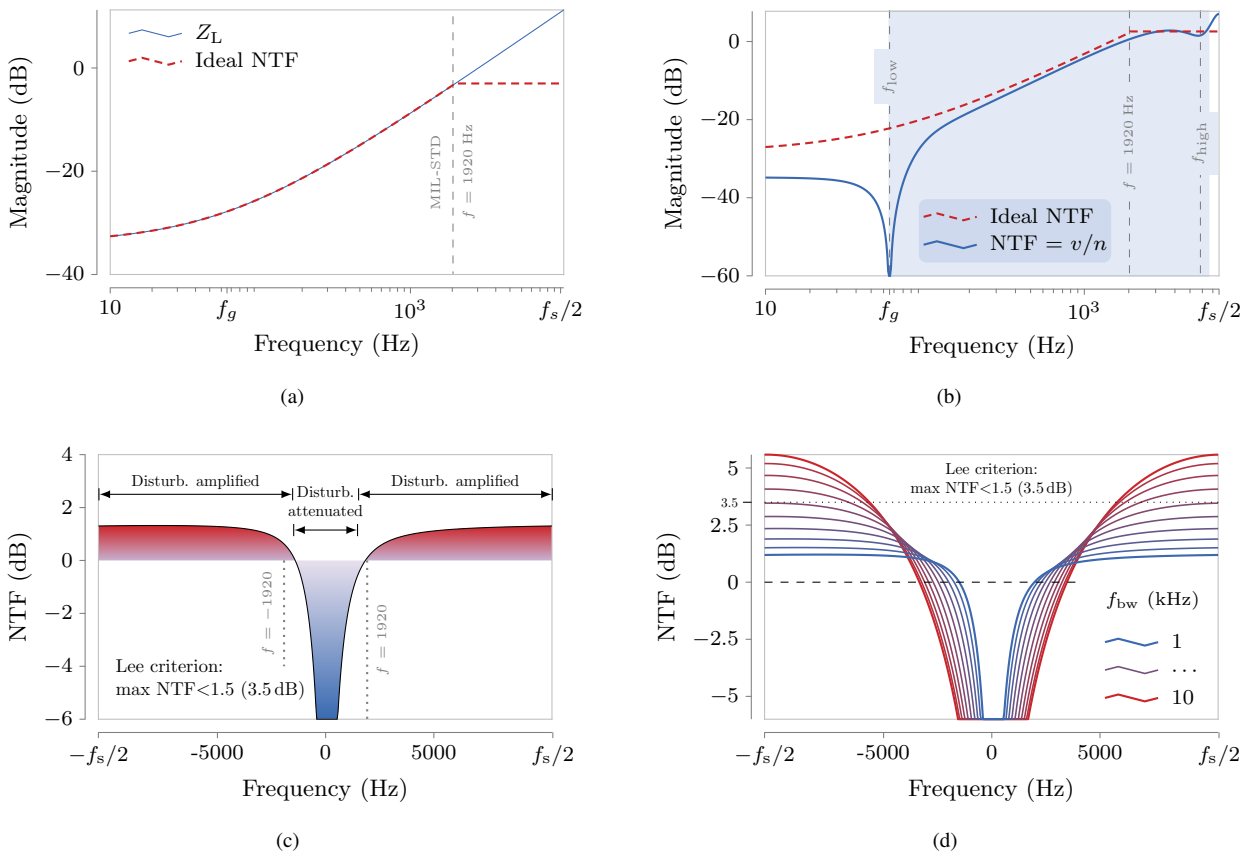

Fig. 7. Plant frequency response and closed-loop disturbance rejection response. (a) Plant response and ideal noise transfer function (NTF). (b) Proposed NTF and ideal NTF. (c) Graphical illustration of Bode's integral theorem: red frequency regions denote disturbance amplification and blue frequency region denotes disturbance attenuation. (d) Graphical illustration of Bode's integral theorem: variantion in the disturbance attenuation frequency range.

a faster convergence of the grid current to the reference value, at the expense of increasing the controller effort. Conversely, if the value of $\mathbf{Q}$ is reduced, then the controller effort is reduced, a slower response is obtained, and the dynamics of the closed-loop system approach the dynamics of the open-loop plant. However, there is not an analytical expression or a direct quantitative relation between the values of $\mathbf{Q}$ and $\mathbf{R}$ and performance parameters such as the controller reference-tracking bandwidth or the disturbance-rejection bandwidth. By adjusting the magnitude of $\mathbf{R}$ in comparison to the magnitude of $\mathbf{Q}$, the designer can trade off speed of convergence (or bandwidth) for controller effort. This characteristic is illustrated in Fig. 7(c) and Fig. 7(d).

Additionally, the dynamics of the closed-loop system, which are determined by the LQR compensator gain, can also be adjusted by the selected disturbance model, cf. (4) and (5). Since there are several parameters that affect the dynamics, for simplicity, the proposed design method assigns a unity value to $\mathbf{R}$ and to the elements of $\mathbf{Q}$ that weight state-variables related to the grid current. However, the designer still can tune the dynamics of the system by adjusting the value of the gain K_{high} in the disturbance model (5). The state weighting matrix permits to adjust the speed of convergence of each state variable. Among the six system state variables contained in $\mathbf{x}_{\text{sys}}$, only two state variables are directly associated to the grid current. These two state variables are the measured grid current, which is the first variable in the plant state vector $\mathbf{x}_{\text{plant}}$ and the current error filtered by the disturbance model, which is the first variable in the disturbance state vector $\mathbf{x}_{\text{dist}}$. Therefore, the weighting matrix $\mathbf{Q}$ is a diagonal matrix whose entries are zero for all elements other than the elements that multiply the indicated two variables. A unity value is also assigned to the non-zero state weighting matrix elements for simplicity.

$$\mathbf{Q} = \begin{bmatrix} 1 & 0 & 0 & 0 & 0 & 0 \\ 0 & 0 & 0 & 0 & 0 & 0 \\ 0 & 0 & 0 & 0 & 0 & 0 \\ 0 & 0 & 0 & 0 & 0 & 0 \\ 0 & 0 & 0 & 0 & 1 & 0 \\ 0 & 0 & 0 & 0 & 0 & 0 \end{bmatrix}, \tag{16}$$

In order to obtain a good performance, Lee's criterion [31] recommends not exceeding a 50% amplification of disturbances at any frequency. This is a general rule recommended for high order systems. When applied to the proposal, which is a sixth order system, a higher disturbance amplification can potentially be achieved; however, this proposal meets the indicated criterion by adjusting the value of K_{high}.

Fig. 7(b) shows the resultant NTF and compares it to the shape of the previously defined ideal NTF. The proposal follows the shape of the ideal NTF at high frequencies and it exceeds the ideal attenuation at low frequencies. In

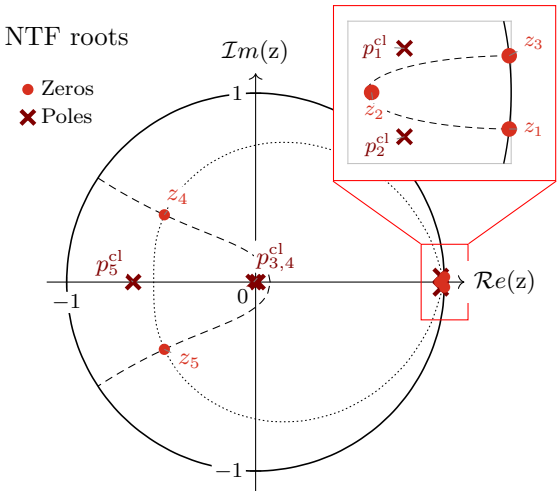

Fig. 8. Pole-zero map of the noise transfer function (NTF).

particular, at the fundamental grid frequency, the proposed NTF design shows an infinite attenuation, as expected from the resonant poles included in the disturbance model. This ensures zero steady-state error in the grid current at such frequency. Fig. 8 shows the resultant pole-zero map of the noise transfer function (NTF). It should be noted that the pole p_5 has a negligible effect in the dynamics of the system in spite of it having a small damping because the transient response associated to this pole decays very fast since it is located at a high frequency, compared to the dominant poles of the system, which are located at lower frequencies.

V. L-Filtered Converter Operation During Weak Grid Conditions

LCL-filtered converters significantly change the grid impedance seen at the PCC at high frequencies, compared to L-filtered converters, due to their relatively low output impedance. Grid voltage notching caused by rectifier loads, such as DC drives, can cause operation problems and/or failures to other equipment, such as an EPS with an AFE, specially when an LCL filter is employed. This problem has been analyzed in the literature [32] and a solution has also been proposed [33]. This solution increases the output impedance of an LCL filtered power converter by adding a novel wide spectrum harmonic filter between the converter and the PCC. However, L-filtered PWM-based converters also experience performance limitations in such conditions. During weak grid conditions the grid impedance seen by a grid-tied inverter at the PCC rises. In this situation, a PWM-based controller has an important limitation compared to the proposal if an L filter is selected to connect the inverter to the grid.

The combined effect of the L coupling filter and the grid impedance forms a voltage divider that attenuates the converter switching noise. The attenuation factor at the PCC is determined by the filter and grid impedance values, cf. Fig. 9(a).

$$\frac{v_{\text{PCC}}}{v_{\text{VSC}}} = \frac{Z_{\text{g}}}{Z_{\text{f}} + Z_{\text{g}}}. \tag{17}$$

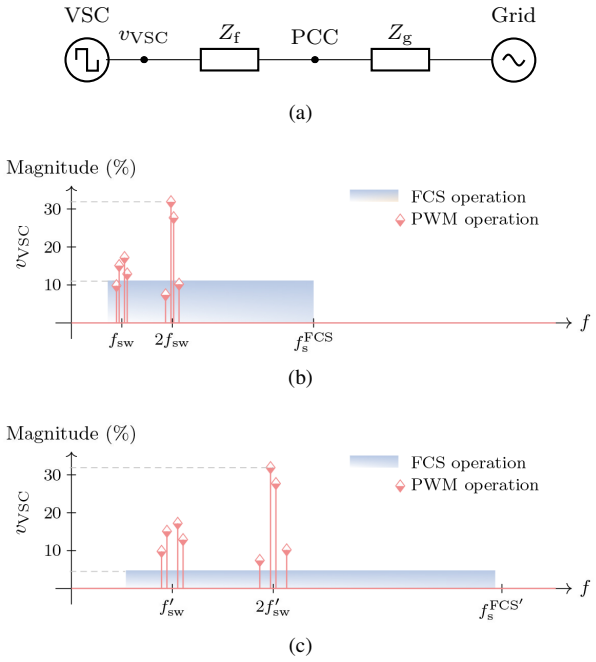

Fig. 9. Simplified model of an L-filtered grid-tied inverter connected to a weak grid with a grid impedance of value Z_{g}. (a) Voltage distortion at the VSC output for a converter with a PWM operating and a modulation index of 0.9 [34, Table 6.4] and a converter that uses a FCS operation. (b) The switching frequency is f_{sw}. (c) The switching frequency is $f'_{\text{sw}} = 2f_{\text{sw}}$.

At high frequencies, the impedance is mainly inductive; therefore, the attenuation factor is constant.

$$\frac{v_{\text{PCC}}}{v_{\text{VSC}}} = \frac{L_{\text{g}}}{L_{\text{f}} + L_{\text{g}}}. \tag{18}$$

Since the attenuation does not increase with frequency, it is not possible to reduce the amplitude of switching voltage harmonics at the PCC generated in an L-filtered VSC with a PWM by increasing the switching frequency. In fact, if the switching frequency is increased and the L filter value is reduced, the switching noise at the point of common coupling will always increase when a PWM operation is employed. This limits the application of novel semiconductor developments to L-filtered converters with a PWM, which continue to increase the switching frequency of semiconductor devices and reduce the size and weight of filter elements. Conversely, the proposal spreads the switching noise throughout a frequency range that increases with the switching frequency. The amplitude of the switching noise at the point of common coupling is reduced as the frequency increases, as illustrated in Fig. 9(b) and Fig. 9(c). As a result, compliance with harmonic regulation is improved without having to modify or increase the size of the filter.

VI. Simulation and Experimental Results

This section assesses the performance of the proposed controller and validates the theoretical results previously presented. The tests are conducted both in simulation and experimentally. The simulation results are carried out in a 5-MW VSC working as an AFE with a 1.2-kV dc bus v_{dc} and connected to a 690-V line-to-line 60-Hz three-phase grid. The grid is formed by two 3.6-MVA synchronous generators

TABLE II
MULTIMEGAWATT SETUP PARAMETERS

VSC (base reference)			
Base power	S_{base}		3.4 MVA
Base voltage	V_{base}		690 V
Base frequency	f_{base}		60 Hz
Base impedance	Z_{base}		0.14 Ω
Base inductance	L_{base}		371 μH
Base capacitance	C_{base}		19 mF
Switching frequency	f_{sw}	37.5 p.u.	2.25 kHz
Sampling freq. PWM controller	f_{s}		4.5 kHz
Sampling freq. FCS controller	f_{s}		16 kHz
DC bus voltage	v_{dc}		1200 V_{DC}
LCL filter (PWM-based controller)			
Grid-side inductance	L_1		0.09 p.u.
Converter-side inductance	L_2		0.04 p.u.
Filter capacitance	C_{f}		0.08 p.u.
L filter (proposed FCS controller)			
Inductance	L_{f}		0.13 p.u.
Grid Parameters			
Generator rated voltage	v_{g}		400 $V_{\text{phase}}^{\text{RMS}}$ - 1 p.u.
Generator rated frequency	f_{g}		60 Hz - 1 p.u.
Generator rated power	S_{g}		3.6 MVA - 1.1 p.u.
Generator impedance	X''_{d}		0.08 p.u.
Number of paralleled generators			2 units
Grid impedance	Z_{g}		0.04 p.u.
Grid SCR	SCR		25

operating in parallel. The generators have a synchronous reactance of value 8%. Such impedance results in a grid SCR of value SCR $= Z_{\text{base}}/|Z_{\text{g}}| = 25$, which denotes a weak grid.

The following results compare the performance of the proposal to a PWM-based design. In order to achieve a meaningful comparison, a common switching frequency is established for both designs. The PWM-based controller runs at a sampling frequency of 4.5 kHz using a PWM with a double-update sampling strategy, which results in a 2.25 kHz switching frequency. The proposal is executed at a higher sampling frequency of value 16 kHz in order to achieve the same average switching frequency of 2.25 kHz because the FCS operation yields a lower switching to sampling ratio.

In order to connect the VSC to the grid, the proposal employs an L filter, whereas the PWM-based controller that is implemented for comparison employs an LCL filter. An LCL filter is frequently installed due to its higher attenuation at high frequencies; however, the proposal is able to achieve compliance using just an L filter with an inductance value equal to the total inductance of the LCL filter. The LCL filter impedance values and the remaining setup parameters are listed in Table II. The selected filter impedance values and switching frequency are commonly employed in low-voltage high-power applications with two-level VSCs [35]–[38]. In order to synchronize the VSC with the grid, a synchronous reference frame phase-locked loop (PLL) with additional filtering [39] is implemented.

TABLE III
PROTOTYPE SETUP PARAMETERS

VSC (base reference)			
Base power	S_{base}		5 kVA
Base voltage	V_{base}		400 V
Base frequency	f_{base}		50 Hz
Base impedance	Z_{base}		32 Ω
Base inductance	L_{base}		101 mH
Base capacitance	C_{base}		100 μF
Switching frequency	f_{sw}	37.5 p.u.	1.875 kHz
Sampling freq. PWM controller	f_{s}		3.75 kHz
Sampling freq. FCS controller	f_{s}		14 kHz
DC bus voltage	v_{dc}		700 V_{DC}
LCL filter (PWM-based controller)			
Converter-side inductance	L_1		0.09 p.u.
Grid-side inductance	L_2		0.04 p.u.
Filter capacitance	C_{f}		0.08 p.u.
L filter (proposed FCS controller)			
Inductance	L_{f}		0.13 p.u.
Grid Parameters			
Grid voltage	v_{g}		1.0 p.u.
Grid impedance	L_{g}		0.04 p.u.
Grid SCR	SCR		25

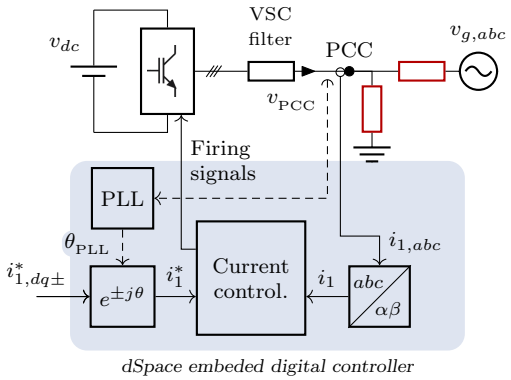

(a)

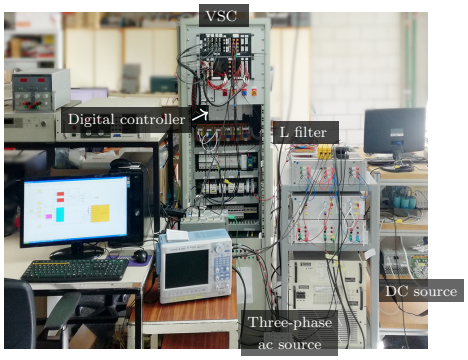

(b)

Fig. 10. Experimental setup. (a) Diagram. (b) Photograph.

The experimental results are carried out using a lower power prototype that is controlled by an embedded hardware

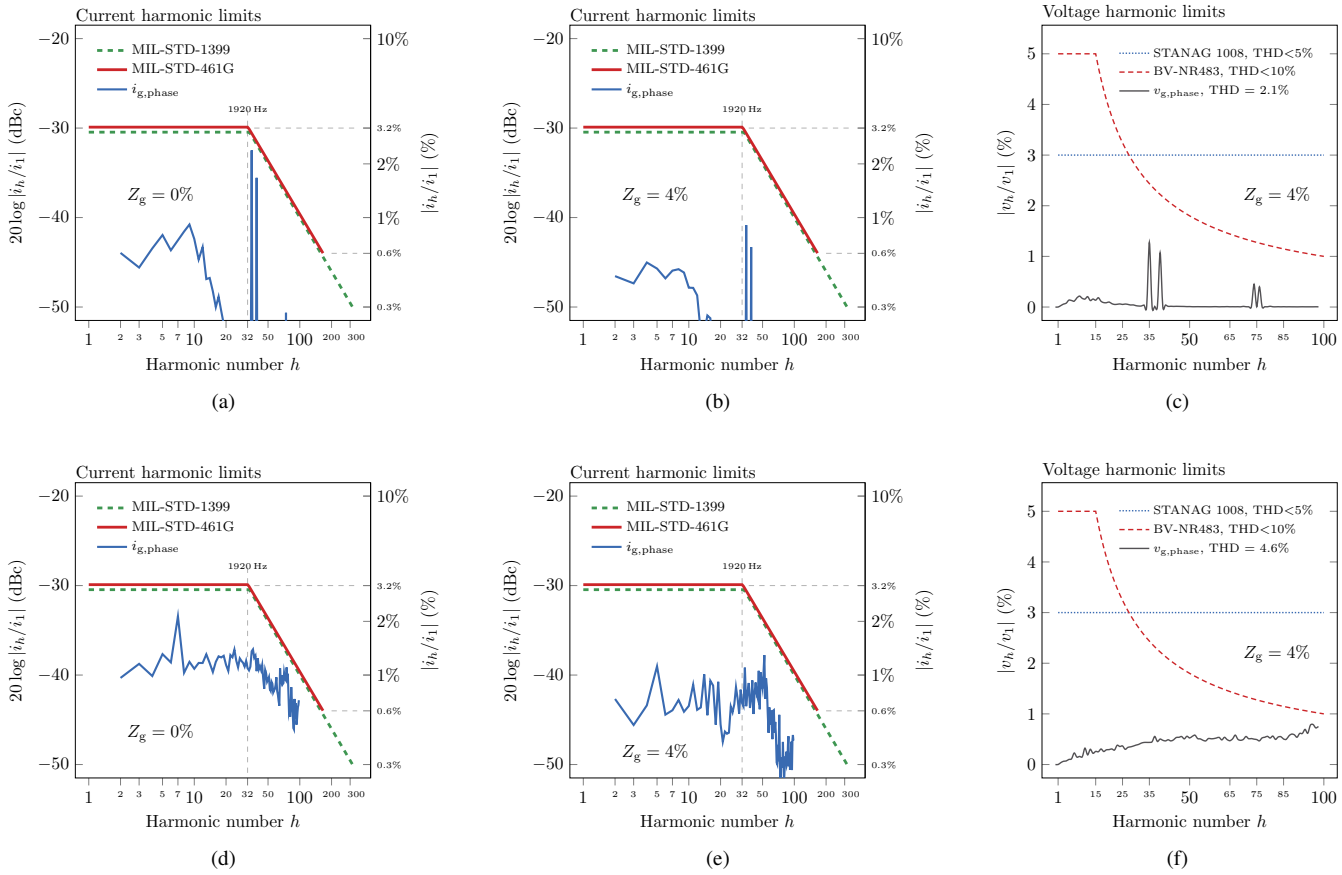

Fig. 11. Simulated current and voltage distortion at the point of common coupling (PCC) and harmonic limits commonly adopted in electrical grids of ships. (a) Current harmonics of a pulse width modulator (PWM)-based current controller with $Z_g = 0\%$. (b) Current harmonics of a pulse width modulator (PWM)-based current controller with $Z_g = 4\%$. (c) Voltage harmonics at the PCC generated by a PWM-based controller with $Z_g = 4\%$. (d) Current harmonics of the proposal with $Z_g = 0\%$. (e) Current harmonics of the proposal with $Z_g = 4\%$. (f) Voltage harmonics at the PCC generated by the proposal with $Z_g = 4\%$.

platform. The platform where the controller is implemented is a MicroAutoBox from the German manufacturer dSPACE with custom signal conditioning modules to interface with the power converter. The same platform was also used to acquire all the measurements shown in the experimental results. This is a rapid prototype embedded control platform that is programmed using Matlab/Simulink graphical programing interface. By using the same numeric computing environment during the controller design process and the experimental hardware test and validation, the implementation process is greatly simplified. The setup parameters of the prototype converter are the same in per unit value as the parameters of the multimegawatt converter. Since the base frequency of the electrical grid in the lab is 50 Hz and the base frequency of the multimegawatt setup is 60 Hz, the VSC switching frequency for the experimental prototype is 1.875 kHz. Therefore, the sampling frequency of the PWM-based controller is 3.75 kHz and the sampling frequency of the proposal is 14 kHz. Table III details all the experimental setup parameters. A simplified block diagram representation and a photograph of the setup is shown in Fig. 10.

The results are organized in three parts. The first part shows the spectral characteristics of the current harmonics generated by the power converter and the resultant voltage harmonics that appear at the PCC due to a non-zero grid impedance, i.e., during weak grid conditions. Both results are compared to the current harmonic limits defined by [15] and [16] and the voltage harmonic limits established in [17] and [18]. The second part shows the transient characteristics of the current controller. Both reference tracking and disturbance rejection responses are analyzed. Finally, the last part assesses the operation of the converter when the grid contains an unmodeled resonance.

Fig. 11, Fig. 13 and Fig. 15 correspond to a simulation of the multimegawatt converter with the setup parameters detailed in Table II. Fig. 12, Fig. 14 and Fig. 16 correspond to the experimental tests carried out in the prototype converter with the setup parameters detailed in Table III.

Fig. 11 and Fig. 12 show the simulated and experimental amplitude of the current and voltage harmonics, respectively, for a PWM-based controller with an LCL filter and compare them to the current and voltage harmonics of the proposal, operating in the same conditions, but using an L filter with the same total inductance as the LCL filter. As shown, the distortion generated by the PWM-based controller is concentrated at a few harmonics located around the switching frequency.

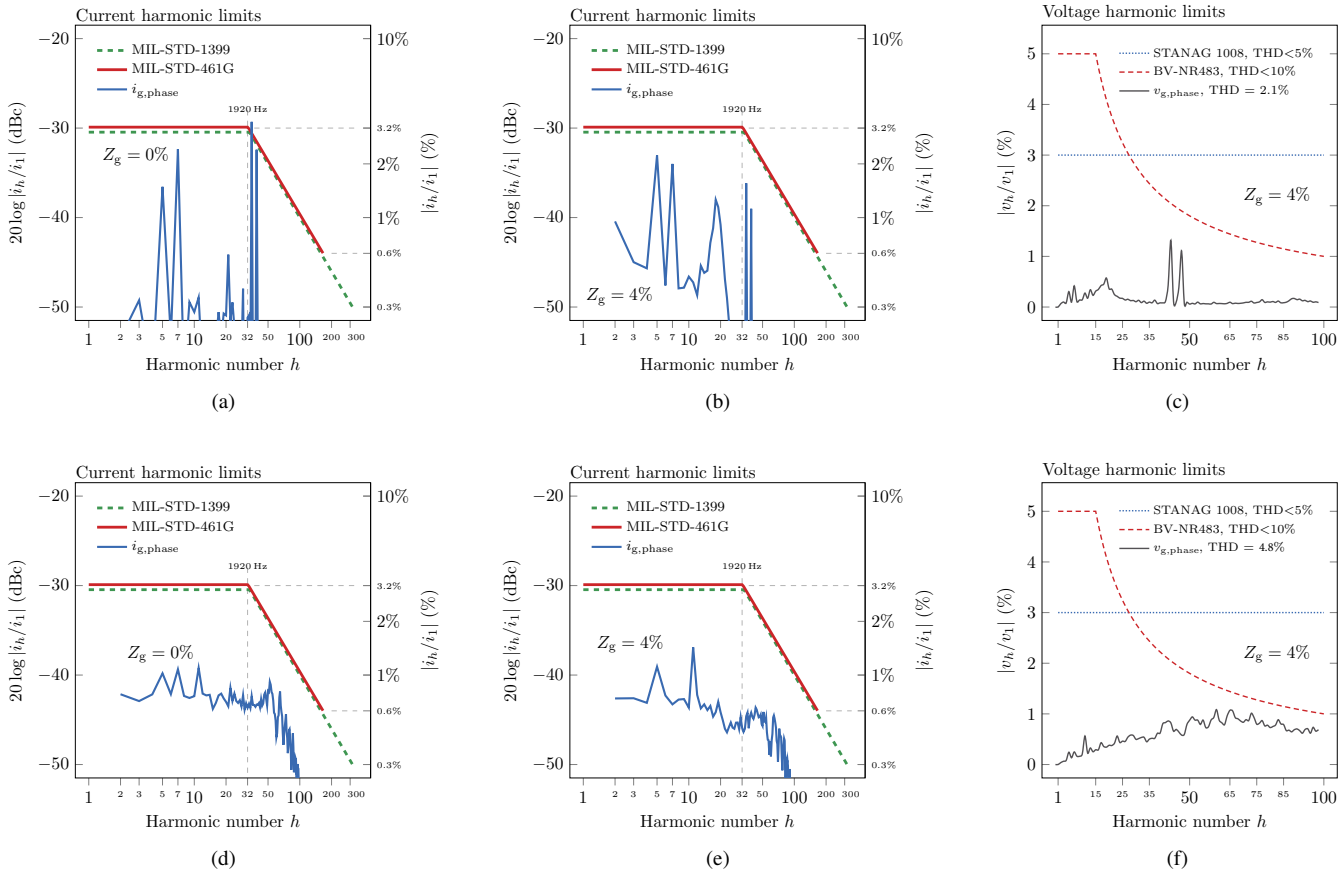

Fig. 12. Experimental current and voltage distortion at the point of common coupling (PCC) and harmonic limits commonly adopted in electrical grids of ships. (a) Current harmonics of a pulse width modulator (PWM)-based current controller with $Z_g = 0\%$. (b) Current harmonics of a pulse width modulator (PWM)-based current controller with $Z_g = 4\%$. (c) Voltage harmonics at the PCC generated by a PWM-based controller with $Z_g = 4\%$. (d) Current harmonics of the proposal with $Z_g = 0\%$. (e) Current harmonics of the proposal with $Z_g = 4\%$. (f) Voltage harmonics at the PCC generated by the proposal with $Z_g = 4\%$.

On the other hand, the proposal spreads the noise throughout a wider frequency range and achieves a lower peak amplitude than the main PWM switching harmonics. Both solutions meet the stringent distortion limits defined by [15]–[18] for individual harmonics during weak grid conditions ($Z_g = 4\%$). However the proposal does not require the capacitors included in the LCL filter. Such change reduces the cost and increases the reliability of the proposal, compared to a PWM-based solution. The PWM-based solution achieves a lower voltage total harmonic distortion (THD) than the proposal, in spite of it having higher individual harmonics, thanks to the higher attenuation provided by the LCL filter at high frequencies. The experimental tests show higher amplitude low-order current harmonics, compared to the simulation results. These low-order current harmonics are caused by the grid low-order distortion and are specially noticeable in the PWM-based solution due to its lower disturbance rejection bandwidth compared to the proposal. If additional resonant controllers tuned at these harmonic frequencies are incorporated to the PWM-based controller, then these harmonics can also be eliminated.

Fig. 13 and Fig. 14 show the simulated and experimental reference tracking response, respectively, of the proposal to a reference step from zero to rated power and compare them to a PWM-based design. In order to assess the dynamic characteristics of the current controller isolated from the dynamics of the DC-voltage controller, a reference step in the q axis is commanded to the current controller. In this manner, a current transient event is generated without affecting the DC voltage. Thanks to the LQR design and the FCS operation of the converter, the proposal achieves a faster response than a PWM-based design. The experimental waveforms contain more noise than the simulated ones due to unmodeled effects in the experimental setup, such as sensors intrinsic noise. Both designs exhibit a high-order transient response. Such high-order dynamics are mainly originated by the high-order controller in the case of the proposal, and the LCL filter in the case of the PWM-based design.

Fig. 15 and Fig. 16 compares the response of both controllers to a type-C sag in the grid voltage. This type of disturbance introduces a negative sequence component in the grid voltage by causing both a drop in amplitude and a shift in the phase of two of the phases of the grid voltage. Similarly to the previous test, in order to assess the transient response to a grid disturbance of the proposal isolated from the dynamics of the DC-voltage controller, the reference to the current

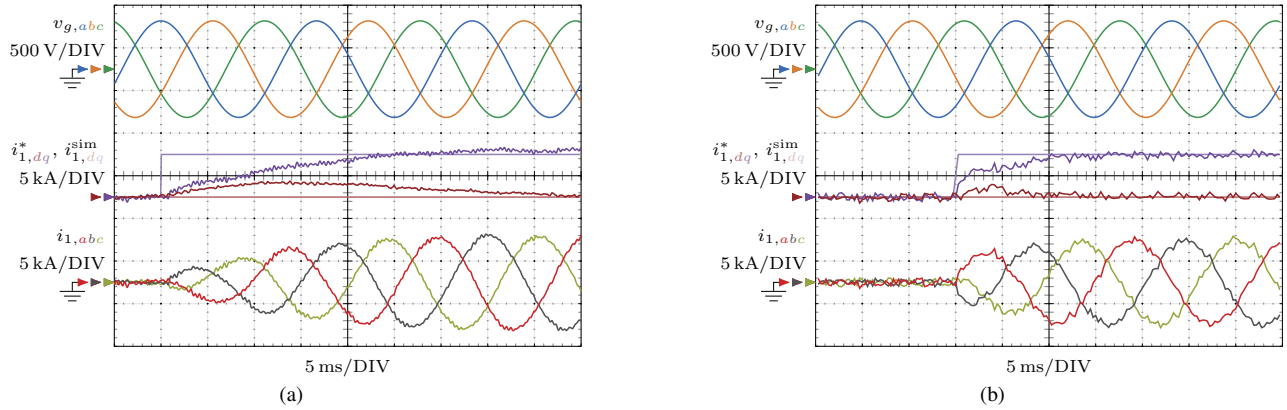

Fig. 13. Simulated waveforms during a 5-kA reference step in the q axis of the +dq frame. Ggrid current in the dq frame $i_{1,\text{dq}}$, in the abc frame $i_{1,\text{abc}}$, and grid voltage v_{g}. (a) Pulse width modulator (PWM)-based controller. (b) Proposal.

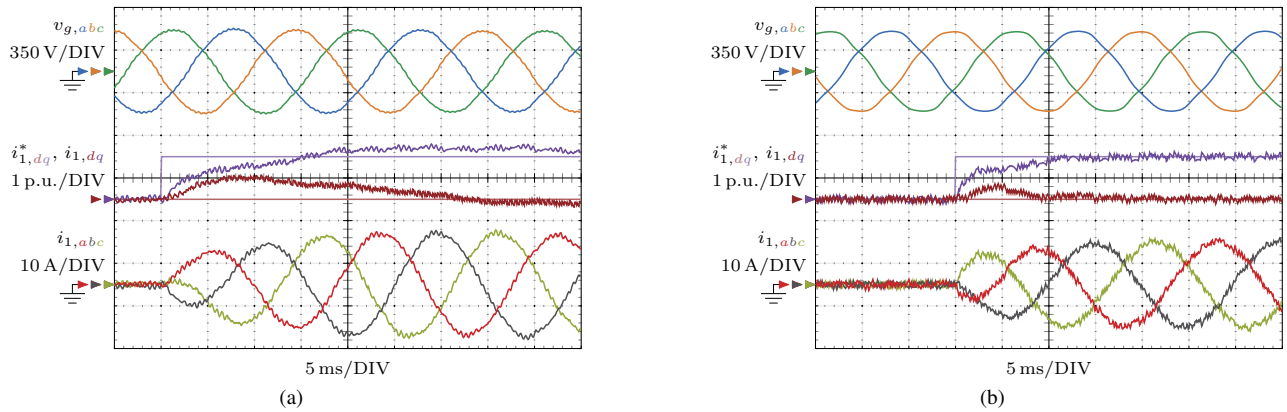

Fig. 14. Experimental waveforms during a 10-A reference step in the q axis of the +dq frame. Measured grid current in the dq frame $i_{1,\text{dq}}$, in the abc frame $i_{1,\text{abc}}$, and measured grid voltage v_{g}. (a) Pulse width modulator (PWM)-based controller. (b) Proposal.

controller is maintained constant. As expected from its fast response, the proposal quickly compensates the sudden voltage disturbance. Moreover, the proposal completely eliminates any steady-state error due to the unbalanced grid voltage thanks to the low frequency resonant controller C_{low} included in the disturbance model. The proposal also contains more high-frequency switching noise during steady-state due to using an L filter instead of the LCL filter used by the PWM-based design.

Fig. 17 and Fig. 18 show the simulated and experimental voltage at the PCC $v_{\text{PCC},abc}$ when the grid contains an unmodeled resonance and the grid-tied inverter is coupled to the grid using an L filter. The amplitude of the grid-current reference i_1^* is set to five amps peak ($i^*_{1,d} = 5$ A and $i^*_{1,q} = 0$ A). The grid resonance is formed by the grid inductance L_g and a capacitive load C_{load} connected at the PCC. The resultant resonance frequency is close to twice the switching frequency of the converter. In order to limit the grid resonance excitation and avoid equipment damage, the VSC dc bus voltage is set an order of magnitude lower than its nominal value and the amplitude of the grid voltage is set to zero in order to avoid overmodulation of the VSC. Thus, the voltage measured at the PCC directly corresponds to the noise distortion caused by the VSC. The results show the proposal excites less the grid resonance compared to the PWM-based controller in the same conditions, as expected from its FCS operation that distributes the switching noise across a wide frequency range, cf. Fig. 9. In the experimental results, there is a larger difference in the resonance amplitude between phases, compared to the simulation results for the PWM-based design. This is due to the effect of small parameter variations, which result in noticeable deviations at high frequencies.

The EPS in the presented application is composed of two independent power converters and two independent propulsion motors; therefore, in the event of a converter fault or a motor fault, operation can be maintained, as required by classification bodies.

VII. Conclusion

This article has presented a linear current controller for its application in the control of the grid side current of an Active Front End used for electric propulsion systems in AC ship microgrids. The proposal does not use a PWM to generate the firing signals; instead, it uses a FCS operation, which eliminates the PWM switching harmonics. In addition, the presented design process reveals a fundamental design trade off that exists between the average switching frequency of the current controller and the lowest current distortion achievable. In marine applications, the proposal offers some advantages. It is able to meet applicable individual harmonic limits using

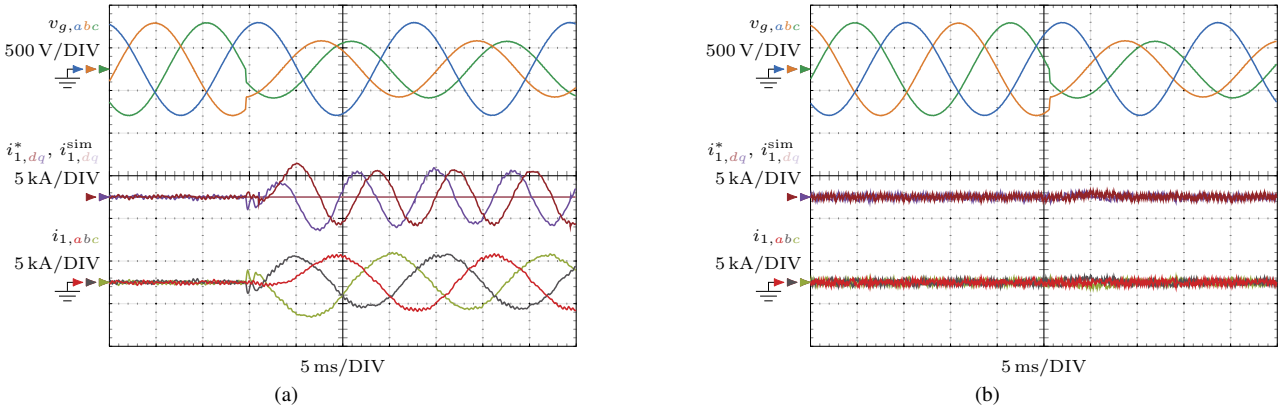

Fig. 15. Simulated waveforms during a 40-ms grid voltage interruption. Grid current in the dq frame $i_{1,\text{dq}}$, in the abc frame $i_{1,\text{abc}}$, and grid voltage v_{g}. (a) Pulse width modulator (PWM)-based controller. (b) Proposal.

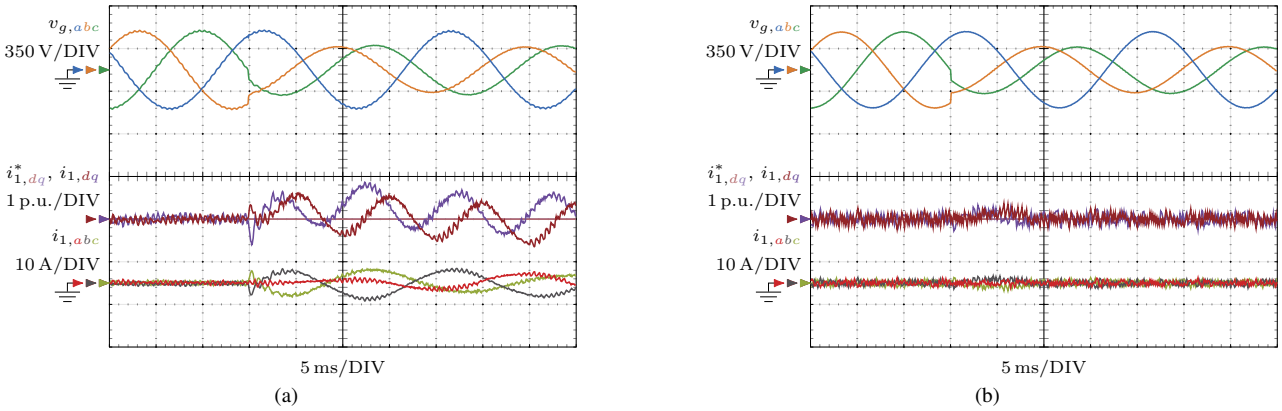

Fig. 16. Experimental waveforms during a type-C grid voltage sag. Measured grid current in the dq frame $i_{1,\text{dq}}$, in the abc frame $i_{1,\text{abc}}$, and measured grid voltage v_{g}. (a) Pulse width modulator (PWM)-based controller. (b) Proposal.

an L filter in place of an LCL filter, without increasing the total filter inductance value or the average switching frequency. The FCS operation results in a high-bandwidth controller, which is able to compensate the switching noise generated by the VSC. Additionally, such high bandwidth provides fast transient dynamics to other grid disturbances such as a voltage sag, without including a grid voltage feedforward in the control. The FCS operation also minimizes the excitation of unmodeled resonances in the grid, which can occur in AES grids depending on the loading conditions. This solution leverages the convenience of linear control theory; hence an stability analysis can be carried out using conventional linear control techniques. Contrarily to other controllers with a FCS operation, such as FCS-MPC, which require more complex nonlinear stability studies including Lyapunov functions, this is a simpler and valuable solution for practicing power-electronic engineers and researchers that are familiar with linear control theory.

References

[1] D. Kumar and F. Zare, "A comprehensive review of maritime microgrids: System architectures, energy efficiency, power quality, and regulations," *IEEE Access*, vol. 7, pp. 67 249–67 277, 2019.

[2] P. Ghimire, D. Park, M. K. Zadeh, J. Thorstensen, and E. Pedersen, "Shipboard electric power conversion: System architecture, applications, control, and challenges [technology leaders]," *IEEE Electrification Magazine*, vol. 7, no. 4, pp. 6–20, 2019.

[3] T. Tarasiuk, S. G. Jayasinghe, M. Gorniak, A. Pilat, V. Shagar, W. Liu, and J. M. Guerrero, "Review of power quality issues in maritime microgrids," *IEEE Access*, vol. 9, pp. 81 798–81 817, 2021.

[4] W. N. Zippler, "Marine electrical applications," *Electrical Engineering*, vol. 78, no. 5, pp. 539–541, 1959.

[5] H. L. Hibbard and W. Hetherington, "Historical review of electrical applications on shipboard," *Journal of the A.I.E.E.*, vol. 44, no. 3, pp. 249–263, 1925.

[6] A. Boveri, F. Silvestro, M. Molinas, and E. Skjong, "Optimal sizing of energy storage systems for shipboard applications," *IEEE Transactions on Energy Conversion*, vol. 34, no. 2, pp. 801–811, 2019.

[7] E. Skjong, T. A. Johansen, M. Molinas, and A. J. Sørensen, "Approaches to economic energy management in diesel–electric marine vessels," *IEEE Transactions on Transportation Electrification*, vol. 3, no. 1, pp. 22–35, 2017.

[8] K. Lai and M. S. Illindala, "Sizing and siting of distributed cloud energy storage systems for a shipboard power system," *IEEE Transactions on Industry Applications*, vol. 57, no. 3, pp. 1935–1944, 2021.

[9] M. Haring, E. Skjong, T. A. Johansen, and M. Molinas, "Extremum-seeking control for harmonic mitigation in electrical grids of marine vessels," *IEEE Trans. Ind. Electron.*, vol. 66, no. 1, pp. 500–508, 2019.

[10] G. Sulligoi, A. Vicenzutti, V. Arcidiacono, and Y. Khersonsky, "Voltage stability in large marine-integrated electrical and electronic power systems," *IEEE Trans. Ind. Appl.*, vol. 52, no. 4, pp. 3584–3594, 2016.

[11] IEEE, "Recommended practice and requirements for harmonic control in electric power systems," *IEEE Std 519-2014*, pp. 1–29, Jun. 2014.

[12] I. A. o. C. S. Lloyd's Register, "Requirements concerning electrical and electronic installations," *UR-E*, pp. 1–67, Dec. 2019.

[13] D. N. Veritas, "Rules for classification ships, part 4 systems and components chapter 8 electrical installations," *DNV GL AS*, pp. 1–191, Jan. 2017.

[14] "Electromagnetic compatibility (EMC) - part 3-4: Limits - limitation of emission of harmonic currents in low-voltage power supply systems for

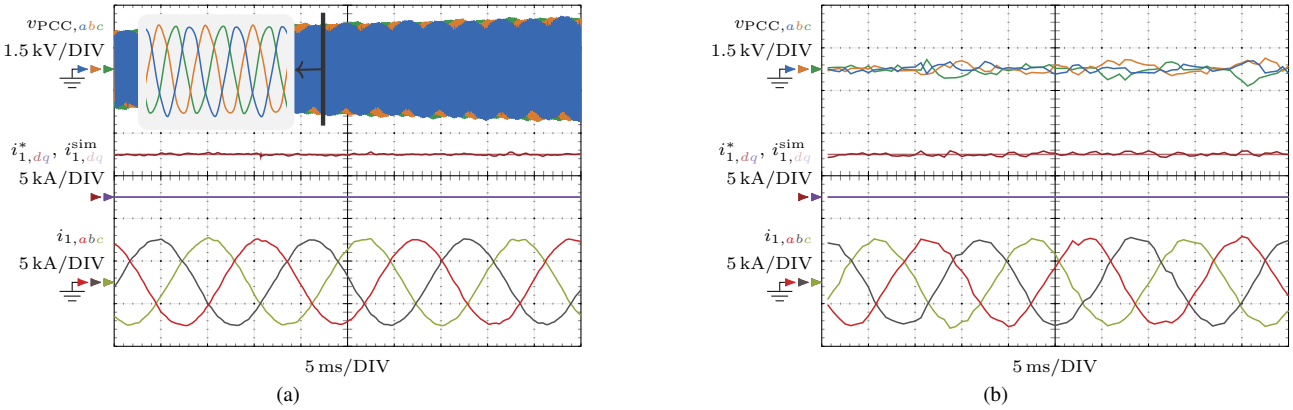

Fig. 17. Simulated voltage distortion at the PCC $v_{PCC,abc}$ and inverter output current i_1 when the grid contains an unmodeled resonance. (a) Pulse width modulator (PWM)-based controller. (b) Proposal.

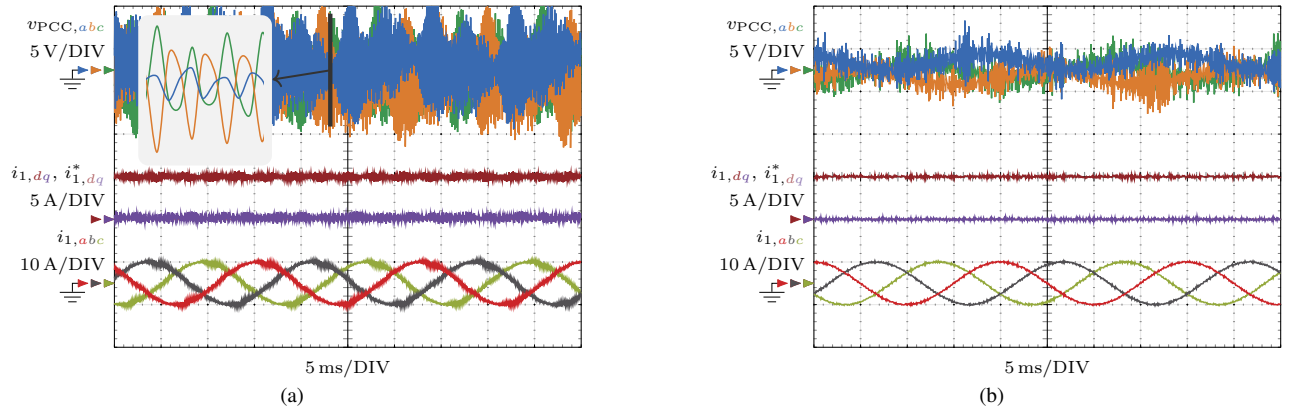

Fig. 18. Experimental voltage distortion at the PCC $v_{PCC,abc}$ and inverter output current i_1 when the grid contains an unmodeled resonance. (a) Pulse width modulator (PWM)-based controller. (b) Proposal.

equipment with rated current greater than 16 a," *IEC 61000-3-4*, pp. 1–29, Oct. 1998.

[15] U. DoD, "Requirements for the control of electromagnetic interference characteristics of subsystems and equipment," *MIL-STD-461G*, pp. 1–280, Dec. 2015.

[16] ——, "Department of defense interface standard section 300b electric power, alternating current," *MIL-STD-1399*, pp. 1–64, Dec. 2008.

[17] NATO, "Characteristics of shipboard low voltage electrical power systems in warships of the nato navies," *STANAG 1008 NAV*, pp. 1–26, Aug. 2004.

[18] B. Veritas, "Rules for the classification of naval ships, part c - machinery, systems and fire protection," *BV-NR 483*, pp. 1–444, Dec. 2017.

[19] P. Karamanakos, E. Liegmann, T. Geyer, and R. Kennel, "Model predictive control of power electronic systems: Methods, results, and challenges," *IEEE Open Journal of Industry Applications*, vol. 1, pp. 95–114, 2020.

[20] S. Vazquez, J. Rodriguez, M. Rivera, L. G. Franquelo, and M. Norambuena, "Model predictive control for power converters and drives: Advances and trends," *IEEE Trans. Ind. Electron.*, vol. 64, no. 2, pp. 935–947, 2017.

[21] P. Karamanakos and T. Geyer, "Guidelines for the design of finite control set model predictive controllers," *IEEE Trans. Power Electron.*, vol. 35, no. 7, pp. 7434–7450, 2020.

[22] D. Pérez-Estévez and J. Doval-Gandoy, "A model predictive current controller with improved robustness against measurement noise and plant model variations," *IEEE Open Journal of Industry Applications*, vol. 2, pp. 131–142, 2021.

[23] ——, "A finite-control-set linear current controller with fast transient response and low switching frequency for grid-tied inverters," *IEEE Trans. Ind. Appl.*, vol. 56, no. 6, pp. 6546–6564, 2020.

[24] A. Hoevenaars, M. Farbis, and M. McGraw, "Active harmonic mitigation: What the manufacturers don't tell you," *IEEE Industry Applications Magazine*, vol. 26, no. 5, pp. 41–51, 2020.

[25] B. Kwak, J.-H. Um, and J.-K. Seok, "Direct active and reactive power control of three-phase inverter for ac motor drives with small dc-link capacitors fed by single-phase diode rectifier," *IEEE Trans. Ind. Appl.*, vol. 55, no. 4, pp. 3842–3850, 2019.

[26] Y. Zhang, J. Jiao, J. Liu, and J. Gao, "Direct power control of pwm rectifier with feedforward compensation of dc-bus voltage ripple under unbalanced grid conditions," *IEEE Trans. Ind. Appl.*, vol. 55, no. 3, pp. 2890–2901, 2019.

[27] T. Dorfling, H. du Toit Mouton, T. Geyer, and P. Karamanakos, "Long-horizon finite-control-set model predictive control with nonrecursive sphere decoding on an FPGA," *IEEE Trans. Power Electron.*, vol. 35, no. 7, pp. 7520–7531, 2020.

[28] G. F. Franklin, J. D. Powell, and M. L. Workman, *Digital Control of Dynamic Systems*, 2nd ed. Addison Wesley Longman, Inc, 1990, p. 261.

[29] S. Pavan, R. Schreier, and G. C. Temes, *Understanding Delta-Sigma Data Converters*, 2nd ed. Wiley-IEEE Press, 2017, p. 584.

[30] G. Stein, "Respect the unstable," *IEEE Control Systems Magazine*, vol. 23, no. 4, pp. 12–25, 2003.

[31] K. C. . Chao, S. Nadeem, W. L. Lee, and C. G. Sodini, "A higher order topology for interpolative modulators for oversampling a/d converters," *IEEE Transactions on Circuits and Systems*, vol. 37, no. 3, pp. 309–318, 1990.

[32] A. H. Hoevenaars, I. C. Evans, and B. Desai, "Preventing ac drive failures due to commutation notches on a drilling rig," *IEEE Transactions on Industry Applications*, vol. 49, no. 3, pp. 1215–1220, 2013.

[33] A. H. Hoevenaars, I. C. Evans, and A. Lawton, "Meeting new marine harmonic standards," in *2008 55th IEEE Petroleum and Chemical Industry Technical Conference*, 2008, pp. 1–9.

[34] D. G. Holmes and T. A. Lipo, *Pulse Width Modulation for Power Converters: Principles and Practice*. IEEE, 2003.

[35] A. A. Rockhill, M. Liserre, R. Teodorescu, and P. Rodriguez, "Grid-filter

design for a multimegawatt medium-voltage voltage-source inverter," *IEEE Trans. Ind. Electron.*, vol. 58, no. 4, pp. 1205–1217, Apr. 2011.
[36] M. Zabaleta, E. Burguete, D. Madariaga, I. Zubimendi, M. Zubiaga, and I. Larrazabal, "LCL grid filter design of a multimegawatt medium-voltage converter for offshore wind turbine using shepwm modulation," *IEEE Trans. Power Electron.*, vol. 31, no. 3, pp. 1993–2001, Mar. 2016.
[37] E. Kantar and A. M. Hava, "Optimal design of grid-connected voltage-source converters considering cost and operating factors," *IEEE Trans. Ind. Electron.*, vol. 63, no. 9, pp. 5336–5347, Sep. 2016.
[38] K. Park, F. D. Kieferndorf, U. Drofenik, S. Pettersson, and F. Canales, "Weight minimization of LCL filters for high-power converters: Impact of PWM method on power loss and power density," *IEEE Trans. Ind. Appl.*, vol. 53, no. 3, pp. 2282–2296, May 2017.
[39] X. Wang, M. G. Taul, H. Wu, Y. Liao, F. Blaabjerg, and L. Harnefors, "Grid-synchronization stability of converter-based resources—an overview," *IEEE Open Journal of Industry Applications*, vol. 1, pp. 115–134, 2020.

Diego Pérez-Estévez (S'15) received the M.Sc. and the Ph.D. degrees from the University of Vigo, Vigo, Spain, in 2014 and 2019, respectively.

Since 2014, he has been with the Applied Power Electronics Technology Research Group. His research interests include control of grid-connected converters and distributed power generation systems.

Jesús Doval-Gandoy (M'99) received the M.S. and Ph.D. degrees in electrical engineering from the Polytechnic University of Madrid, Madrid, Spain, and from the University of Vigo, Vigo, Spain, in 1991 and 1999 respectively.

He is a Professor and the head of the Applied Power Electronics Technology Research Group (APET), University of Vigo. His research interests are in the areas of ac power conversion.

Alberto Crego-Lourido received the M.S. degree in electrical engineering from the University of Vigo, Vigo, Spain, in 1998.

He is the Head of the Electricity Section at Navantia, Ferrol, Spain. His current research interests are in the field of All-Electric Ship.